Chapter 6

'QuoVaDis' model

6.1 Introduction

We introduce the 'QuoVaDis' model, which is the phonetic name for 'CoWaDis', which reminds one that the model incorporates COhesive surfaces, takes into account the WAviness of the free surface and includes 2D DISlocation dynamics. We employ this model based upon the ingredients of the preceding chapters to simulate fatigue crack initiation.

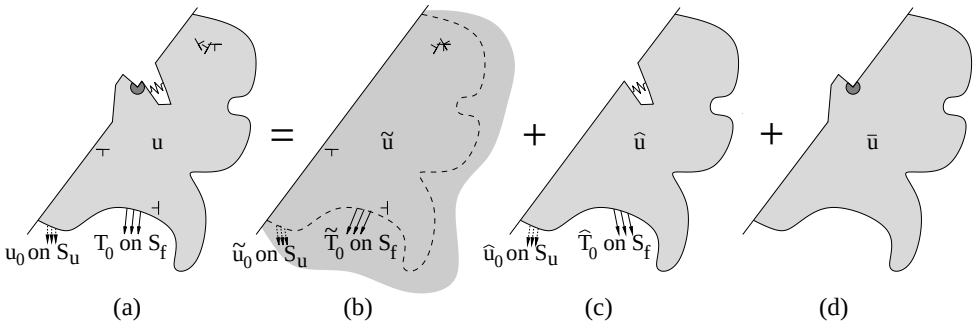

Figure 6.1: 'QuoVaDis' model (a) as the compilation of a dislocation model (b), described in chapter 2, a model to incorporate the cohesive surface and the boundary conditions (c), partially described in chapter 5, and a surface step model (d), developed in chapter 4.

The model splits up the problem we want to analyze, figure 6.1 (a), into three parts. The first part is the 2DD model described in chapter 2. This part models the structuring of dislocations and their collective stress fields and is shown in figure 6.1 (b).

The cohesive surface as well as the boundary conditions are included into the model

through the second part, figure 6.1(c). The cohesive surface model is described in this chapter. Since the cohesive surface law is nonlinear, the boundary value problem is being formulated as an incremental problem using forward Euler time integration. Furthermore, we assume a reversible cohesive surface law, since we neglect oxidation and all other processes, which alter the evolving crack suface and prevent it from healing.

The third part is the approximate description of the fields caused by surface steps, as developed in chapter 4. This is included to account for the influence of surface steps on fatigue.

The three parts are coupled by their elastic fields in a way that is described in section 6.3. The cohesive surface has not been discussed at all so far, so we therefore start this chapter with that.

6.2 Cohesive surface theory

To model cleavage, the cohesive surface model of Xu and Needleman [29] is adopted. This cohesive law couples normal and tangential separation and thus is an extension of the universal binding law by Rose et al. [58], which only includes normal separation.

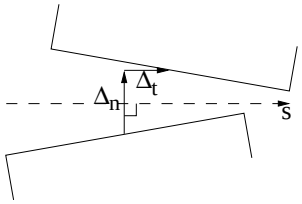

Figure 6.2: Definitions used for the cohesive surface

As shown in figure 6.2, Δ_n denotes the normal separation and Δ_t the tangential separation in the reference configuration. The work of normal and tangential separation is denoted by Φ_n and Φ_t, respectively, and the characteristic lengths are denoted by δ_n and δ_t, respectively. The traction vector $\mathbf{T}$, with components T_n and T_t, is determined by the cohesive energy Φ through

$$\mathbf{T} = -\frac{\partial \Phi}{\partial \mathbf{\Delta}} \tag{6.1}$$

where

$$\Phi = \Phi_n - \Phi_n \exp\left(-\frac{\Delta_n}{\delta_n}\right)\left[\left(1 - r + \frac{\Delta_n}{\delta_n}\right)\frac{1-q}{r-1} - \left(q + \frac{r-q}{r-1}\frac{\Delta_n}{\delta_n}\right)\exp\left(-\frac{\Delta_t^2}{\delta_t^2}\right)\right]$$

The material parameters q and r govern the coupling between the normal and tangential response as

$$\Phi_n = \mathrm{e}\sigma_{\max}\delta_n \tag{6.2}$$
$$\Phi_t = \sqrt{\mathrm{e}/2}\tau_{\max}\delta_t \tag{6.3}$$
$$q = \frac{\Phi_t}{\Phi_n} \tag{6.4}$$
$$r = \frac{\Delta_n^*}{\delta_n} \tag{6.5}$$

where $\mathrm{e} = \exp(1)$ and Δ_n^* is the value of Δ_n after complete shear separation with $T_n \to 0$ (cf. r in figure 6.3 (a)). The traction-separation relations are given by

$$T_n = -\frac{\partial\Phi}{\partial\Delta_n} \tag{6.6}$$
$$= \frac{\Phi_n}{\delta_n}\exp\left(-\frac{\Delta_n}{\delta_n}\right)\left[\frac{\Delta_n}{\delta_n}\exp\left(-\frac{\Delta_t^2}{\delta_t^2}\right) + \frac{1-q}{r-1}\left(1-\exp\left(-\frac{\Delta_t^2}{\delta_t^2}\right)\right)\left(r-\frac{\Delta_n}{\delta_n}\right)\right]$$
$$T_t = -\frac{\partial\Phi}{\partial\Delta_t} \tag{6.7}$$
$$= 2\frac{\Phi_n}{\delta_t}\exp\left(-\frac{\Delta_n}{\delta_n}\right)\left(q+\frac{r-q}{r-1}\frac{\Delta_n}{\delta_n}\right)\frac{\Delta_t}{\delta_t}\exp\left(-\frac{\Delta_t^2}{\delta_t^2}\right)$$

and figure 6.3 shows the corresponding graphs. $\sigma_{\max}$ and $\tau_{\max}$ are the normal and tangential strengths, respectively.

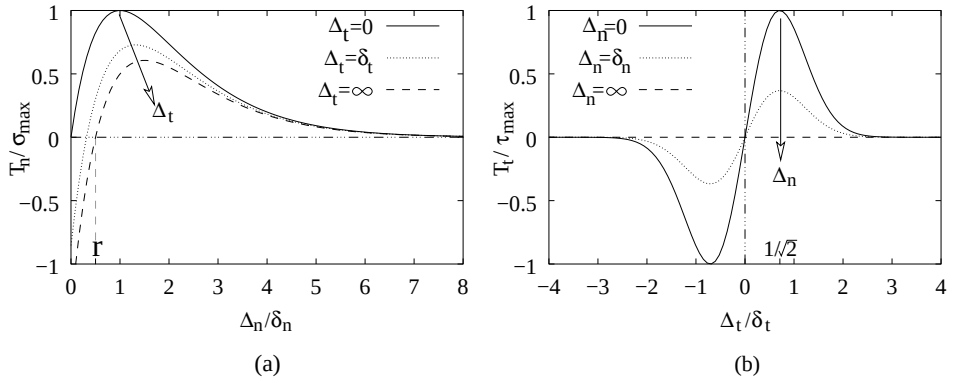

Figure 6.3: Traction-separation law for normal (a) and tangential direction (b) normalized by the maximal normal $\sigma_{\max}$ and tangential stress $\tau_{\max}$.

Let us first focus on the normal traction response for $\Delta_t = 0$ shown in figure 6.3. At small Δ_n the normal traction is increasing almost linearly with increasing normal separation. Thereafter, the slope is decreasing and the maximal normal traction $\sigma_{\max}$ is reached at the characteristic opening δ_n. Afterwards, the traction is decreasing and asymptotically approaches zero when a fully open crack is formed. With increasing tangential separation the maximal normal stress decreases and reaches a non-zero value for complete tangential separation, provided $q < 1$.

The tangential traction – separation curve exhibits the same qualitative behavior as for the normal direction with a maximum of $\tau_{\max}$ reached at $1/\sqrt{2}\delta_t$ but is antisymmetric. Also, under complete normal separation, there is no tangential strength left.

Figure 6.4 shows the influence of the parameters r and q. Figure 6.4 (a) shows that with $r = q$, for increasing normal opening the tangential strength decreases, which can be physically explained by atomic planes being separated and therefore having less resistance for shearing. If $r - q > 0$ the same behavior is seen under compression, but for tension the tangential strength becomes negative, which is unphysical. For $r - q < 0$, there is a maximum in the compressive area, which leads to a lower tangential strength for greater compression, which also is not physical. These observations lead to taking $r = q$. Given this, figure 6.4 (b) shows how the normal strength on the tangential separation. In the limit when the atomic planes are infinitely sheared the maximal normal stress decreases to $(1 - q)\sigma_{\max}$.

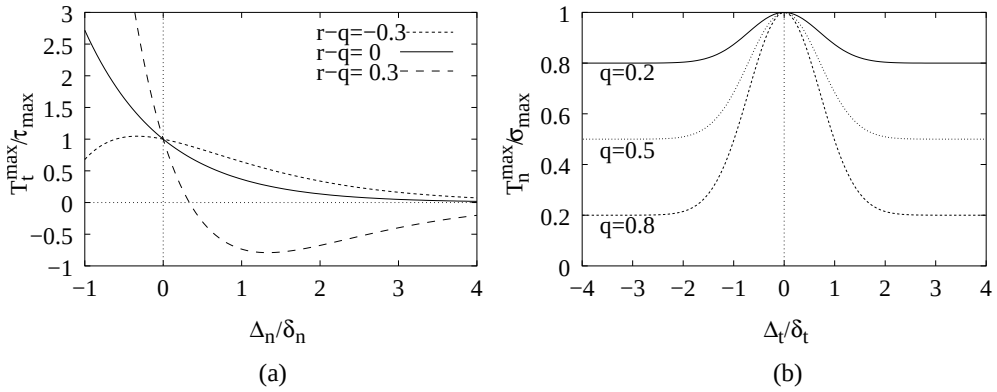

Figure 6.4: Influence of the parameters r and q on the cohesive surface laws (6.6) and (6.7). $T_t^{\max}$ and $T_n^{\max}$ are the tangential and normal strength. While $\tau_{\max}$ and $\sigma_{\max}$ are the corresponding strengths with opening $\Delta_n = 0$ and $\Delta_t = 0$, respectively.

6.3 Boundary value problem

The elastic fields of the body containing the dislocations are calculated, as shown in figure 6.2, by superposition of the elastic fields of the dislocation distribution ˜ described in section 5.2, the ˆ fields, which correct the boundary conditions and the elastic fields due to the surface roughness ¯:

$$\begin{aligned}\boldsymbol{\sigma} &= \tilde{\boldsymbol{\sigma}} + \hat{\boldsymbol{\sigma}} + \bar{\boldsymbol{\sigma}},\\ \boldsymbol{u} &= \tilde{\boldsymbol{u}} + \hat{\boldsymbol{u}} + \bar{\boldsymbol{u}}.\end{aligned}$$

The boundaries, at which the boundary conditions are prescribed, are sufficiently far away that the elastic fields due to the surface roughness can be neglected. Therefore, the ˆ fields correct only for the elastic fields caused by the dislocation distribution:

$$\hat{\boldsymbol{T}} = \boldsymbol{T} - \tilde{\boldsymbol{T}}, \qquad\qquad \hat{\boldsymbol{u}} = \boldsymbol{u} - \tilde{\boldsymbol{u}}.$$

The virtual work for an elastic body with a cohesive surface, neglecting body forces and surface tension, can be written as

$$\int_V \boldsymbol{\sigma}\,\delta\boldsymbol{\varepsilon}\,dV - \int_{S_{\mathrm{coh}}} \boldsymbol{T}\,\delta\boldsymbol{\Delta}\,dS = \int_{S_{\mathrm{ext}}} \boldsymbol{T}\,\delta\boldsymbol{u}\,dS. \tag{6.8}$$

Here, $\boldsymbol{\sigma}$ and $\boldsymbol{\varepsilon}$ are the components of the stress and strain tensor, respectively. V is the volume of the analyzed body, and S_{cos} and S_{ext} are the cohesive and external surface, respectively. $\boldsymbol{\Delta}$ is the separation vector of the cohesive surface, described in the previous section. Naturally, $\boldsymbol{\Delta}$ is evaluated in the deformed configuration. $\boldsymbol{T}$ is the surface traction related to the surface normal $\boldsymbol{n}$ by $\boldsymbol{T} = \boldsymbol{\sigma}\boldsymbol{n}$.

In addition to equation (6.8) at time t, we also consider the virtual work expression at $t+\Delta t$. The equilibrium of the ˜ fields is already enforced through the analytic expressions, as mentioned in section 5.2. Moreover, as described above, the external boundary conditions are corrected for by the finite element method. The volume integral can thus be rewritten in ˆ form:

$$\int_V \hat{\boldsymbol{\sigma}}^{(t+\Delta t)}\,\delta\boldsymbol{\varepsilon}\,dV - \int_{S_{\mathrm{coh}}} \boldsymbol{T}^{(t+\Delta t)}\,\delta\boldsymbol{\Delta}\,dS = \int_{S_{\mathrm{ext}}} \hat{\boldsymbol{T}}^{(t+\Delta t)}\,\delta\boldsymbol{u}\,dS \tag{6.9}$$

Cleveringa et al. [2] gave the Taylor expansion for the cohesive tractions about $t+\Delta t$ for all surfaces:

$$\begin{aligned}\mathbf{T}\left(\boldsymbol{\Delta}^{(t+\Delta t)}\right) &= \mathbf{T}\left(\tilde{\boldsymbol{\Delta}}^{(t+\Delta t)} + \hat{\boldsymbol{\Delta}}^{(t+\Delta t)}\right) = \mathbf{T}\left(\tilde{\boldsymbol{\Delta}}^{(t+\Delta t)} + \hat{\boldsymbol{\Delta}}^{(t)} + \Delta t\,\dot{\hat{\boldsymbol{\Delta}}}\right)\\ &\cong \mathbf{T}\left(\tilde{\boldsymbol{\Delta}}^{(t+\Delta t)} + \hat{\boldsymbol{\Delta}}^{(t)}\right) + \mathbf{K}\left(\tilde{\boldsymbol{\Delta}}^{(t+\Delta t)} + \hat{\boldsymbol{\Delta}}^{(t)}\right)\Delta t\,\dot{\hat{\boldsymbol{\Delta}}}\end{aligned} \tag{6.10}$$

where $\mathbf{K}$ is defined by

$$\mathbf{K} = \frac{\partial \mathbf{T}}{\partial \boldsymbol{\Delta}}$$

$\mathbf{T}$ is the traction vector, while $\boldsymbol{\Delta}$ is the separation vector. Recall that the superposed dot denotes differentiation with respect to time t. Approximating the stresses at $t + \Delta t$ to first order gives

$$\hat{\boldsymbol{\sigma}}^{(t+\Delta t)} = \hat{\boldsymbol{\sigma}}^{(t)} + \dot{\hat{\boldsymbol{\sigma}}}\, \Delta t. \tag{6.11}$$

Substituting equations (6.10) and (6.11) into (6.9) gives the following equation:

$$\int_V \dot{\hat{\boldsymbol{\sigma}}}^{(t)} \delta\boldsymbol{\varepsilon}\, dV - \int_{S_{coh}} \boldsymbol{K} \left(\tilde{\boldsymbol{\Delta}}^{(t+\Delta t)} + \hat{\boldsymbol{\Delta}}^{(t)} \right) \dot{\hat{\boldsymbol{\Delta}}}\, \delta\boldsymbol{\Delta}\, dS - \int_{S_{ext}} \hat{\boldsymbol{K}} \left(\tilde{\boldsymbol{u}}^{(t+\Delta t)} + \hat{\boldsymbol{u}}^{(t)} \right) \dot{\hat{\boldsymbol{u}}}\, \delta\boldsymbol{u}\, dS$$

$$=$$

$$-\frac{1}{\Delta t} \Big[\int_V \hat{\boldsymbol{\sigma}}^{(t)} \delta\boldsymbol{\varepsilon}\, dV - \int_{S_{coh}} \boldsymbol{T} \left(\tilde{\boldsymbol{\Delta}}^{(t+\Delta t)} + \hat{\boldsymbol{\Delta}}^{(t)} \right) \delta\boldsymbol{\Delta}\, dS - \int_{S_{ext}} \hat{\boldsymbol{T}} \left(\tilde{\boldsymbol{u}}^{(t+\Delta t)} + \hat{\boldsymbol{u}}^{(t)} \right) \delta\boldsymbol{u}\, dS \Big]$$

Along the external boundary where tractions are prescribed, we invoke $\boldsymbol{T} = \mathbf{0}$. Additionally, the contribution of the dislocation distribution $\tilde{\boldsymbol{T}} = \mathbf{0}$ here, since we employ the half-space solution for the elastic fields of dislocations. Therefore, $\hat{\boldsymbol{T}} = \mathbf{0}$ along the external surface S_{ext} where tractions are prescribed. Furthermore, we invoke $\delta\boldsymbol{u} = \mathbf{0}$ on the external surface where the displacements are prescribed. In conclusion, all contributions from the external surface vanish. Furthermore, substituting equation (6.8) for the volume integral on the right-hand side and rearranging, one obtains

$$\begin{aligned} &\int_V \dot{\hat{\boldsymbol{\sigma}}}^{(t)} \delta\boldsymbol{\varepsilon}\, dV - \int_{S_{coh}} \boldsymbol{K} \left(\tilde{\boldsymbol{\Delta}}^{(t+\Delta t)} + \hat{\boldsymbol{\Delta}}^{(t)} \right) \dot{\hat{\boldsymbol{\Delta}}}\, \delta\boldsymbol{\Delta}\, dS = \\ &\frac{1}{\Delta t} \Big[\int_{S_{coh}} \left[\boldsymbol{T} \left(\tilde{\boldsymbol{\Delta}}^{(t+\Delta t)} + \hat{\boldsymbol{\Delta}}^{(t)} \right) - \boldsymbol{T} \left(\tilde{\boldsymbol{\Delta}}^{(t)} + \hat{\boldsymbol{\Delta}}^{(t)} \right) \right] \delta\boldsymbol{\Delta}\, dS \end{aligned} \tag{6.12}$$

The first line of equation (6.12) forms the left-hand side of the linear system of finite element equations $Ku = f$ after some derivations. The second line is the change in energy due to the cohesive surface opening.

To incorporate the boundary conditions of the $\tilde{}$ fields in the incremental forward Euler time integration, we rewrite the tractions on the surfaces due to the dislocation distribution as a function of the dislocation velocity:

$$\frac{d\boldsymbol{T}(\tilde{u})}{dt} = \frac{d\boldsymbol{T}(\tilde{u})}{ds} \frac{ds}{dt} = \sum_{disl} \frac{d\boldsymbol{T}_i(\tilde{u})}{ds} v_i$$

Together with equation (6.12) the solution to the rate boundary value problem is defined, which is used in the QuoVaDis model. In addition to the influence of the dislocations, the displacement due to the surface roughness is incorporated into the model in a similar fashion.

6.4 Problem formulation

We use the QuoVaDis model with a random distribution of sources and obstacles. Moreover, we use the analytical approximation to the elastic fields of the surface steps, as described in chapter 4. Initially, the surface is perfectly flat.

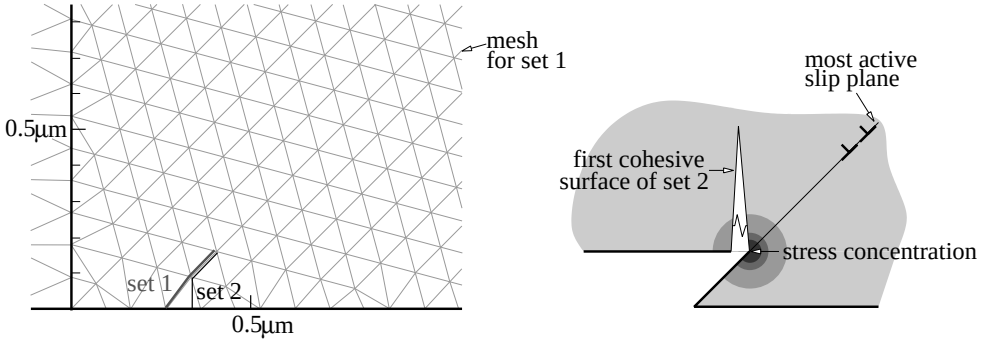

Figure 6.5: Lower left-hand corner of a $2 \times 2\mu\mathrm{m}$ grain with two sets of cohesive surfaces (a). Schematic representation of first cohesive surface at intersection of most active slip plane with free surface (b).

For different random distributions of dislocation sources and obstacles in a $2\mu\mathrm{m} \times 2\mu\mathrm{m}$ grain we have observed the highest stresses at the surface due to the dislocation distribution between $x = 0$ and $x = 0.7\mu\mathrm{m}$. One particular configuration was discussed in chapter 2. We place 12 different sets of cohesive elements in this high stressed area. We employ here the two sets shown in figure 6.5 (a) that fracture in the given time. They differ in the orientation of the cohesive element to the free surface, so that we can investigate the sensitivity of the direction of crack initiation. Both cohesive elements of the first set are oriented along the primary slip system, i.e. 45° to the free surface.

The first cohesive element of set 2 is normal to the free surface, because the stress normal to this cohesive element is maximum in this configuration. The second cohesive element is taken to follow the primary slip system. Furthermore, the first cohesive element is placed at the intersection of the most active slip plane with the free surface, as shown in figure 6.5 (b). Therefore, the stress concentration caused by the surface roughness is maximal for this cohesive element. Additionally, we choose a material with a lower normal fracture energy. In conclusion, this is the 'worst case' scenario.

In both simulations, we use the material parameters $r = q = 0.5$ in equations (6.6) and (6.7), which have been used previously to model fatigue crack propagation [2]. The critical normal opening δ_n is $4b$ and $2b$ for set 1 and 2, respectively. The tangential opening $\delta_t = 4b$ for both sets. The strength of the cohesive surface $\sigma_{\max} = 600\mathrm{MPa} = 6\sigma_{\mathrm{yield}} = 4\sigma_{\mathrm{applied}}$, where σ_{yield} is derived from the average Frank-Read source strength.

Shearing along a slip system produces dislocation motion. However, it does not damage the material, i.e. it does not reduce the normal strength of the cohesive surface. Therefore, if a cohesive element is parallel to a slip system, e.g. the cohesive elements of set 1, we do not allow for any tangential opening of the cohesive element, i.e. we enforce $\Delta_t = 0$. The cohesive element therefore retains its unchanged normal stress-separation law. For cohesive elements that are normal to the free surface the interaction between normal and tangential modes is modeled according to equations (6.6) and (6.7).

We use a small-strain formulation for the description of the dislocation fields and the finite element correction, i.e. the coordinates are given in the undeformed configuration. However recall from the previous section, the cohesive surface opening is calculated in the deformed configuration. This difference in the configurations leads to a problem when calculating the opening of the cohesive element, because the cohesive element is moving relative to the slip planes. While at time t the cohesive element is one side of the slip plane, and the displacement jump due to dislocations on that plane, in the next time step the endpoints of the cohesive element might be on either side of the displacement jump, as shown in figure 6.6. In this case the opening at these endpoints changes significantly from one time step to the next. Depending on the amount of slip, this change can be a multiple of the critical openings δ_n and δ_t. Special rules were developed for this case to prevent a non-continuous change in the opening of the cohesive element and therefore in the stiffness matrix.

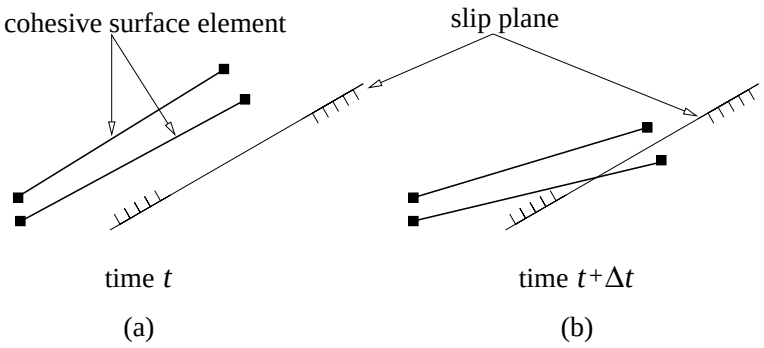

Figure 6.6: At time t, slip plane and cohesive element (a) and at time $t + \Delta t$, cohesive element intersects slip plane, i.e. two opposing nodes (■) of a cohesive element are on either side of the slip plane, causing a problem (b).

Closure of the surfaces during cycling is taken into account implicitly in the cohesive law (6.6) and (6.7). If the normal opening becomes negative the stiffness increases exponentially. This behavior can be explained physically as follows. Both rows of atoms, which are modeled through the edges of the cohesive surface, are physically not able to penetrate or to cross each other. Therefore, the stiffness increases for negative openings.

6.5 Results

In figure 6.7 the normal opening of the cohesive element at the free surface is shown as a function of time for the second set of cohesive elements. Additionally, the envelope of this opening, i.e. the connection of the maximum openings per cycle, is shown. The opening

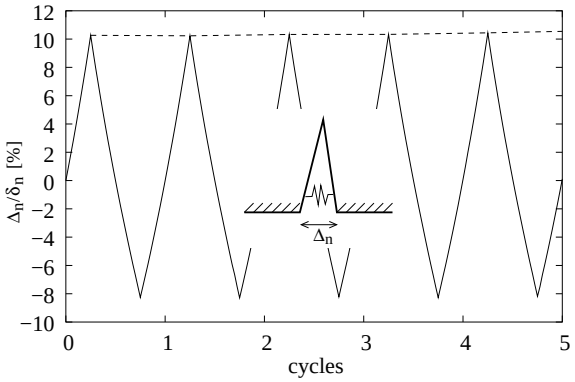

Figure 6.7: The normal opening of the cohesive element Δ_n at the free surface. The model is used for a $2\mu\mathrm{m} \times 2\mu\mathrm{m}$ grain and with the second set of cohesive elements. 100% equals the critical opening δ_n.

in the compressive phase is smaller (in absolute value) than in the tensile phase. This is due to the exponential increase in the stiffness of the cohesive element for negative normal openings.

The normal opening of the cohesive element at the free surface for both sets as a function of time over many cycles is shown in figure 6.8 (a). The opening for the second set is almost constant initially and then increases rapidly until fracture initiates after ~ 36 cycles. We stop the simulation once the normal opening Δ_n has reached the critical normal opening δ_n of the cohesive element and refer to this event as 'fatigue crack initiation'. At this point, the deformed mesh, i.e. the atomic structure, is highly distorted and dislocations are assumed to be unable to glide across the cohesive surface. Therefore, additional rules for the dislocation motion would be necessary whenever the cohesive element has an opening greater than δ_n. Moreover, dislocations moving into an open cohesive surface would produce a surface step in the flanks of the evolving crack. This cohesive surface roughness would prevent closure of the cohesive surface. All these additional rules would further complicate the model. In these simulations we terminate the simulation once $\Delta_n = \delta_n$.

For the first set of cohesive elements, initially the maximum normal opening grows slowly and then the opening increases rapidly during cycle 140, figure 6.8 (a). Afterwards, the maximum opening increases slowly again but with a larger amplitude for a few cycles. In cycles 142 the normal opening reaches 93% of the critical opening and afterwards 100%. We note that the amplitude of the opening is constant until cycle 140. However, the average

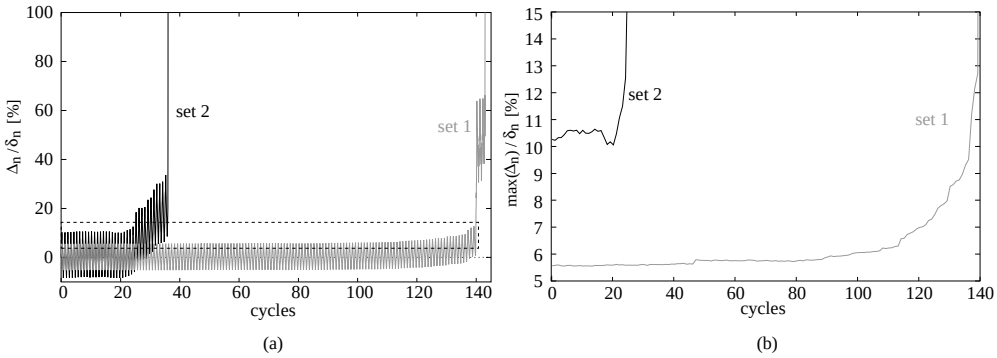

Figure 6.8: Normal opening at the free surface (a). Zoom into the dashed box of (a) showing only the maximum normal opening per cycle (b) for both sets of cohesive elements in a $2\mu\mathrm{m} \times 2\mu\mathrm{m}$ grain.

opening per cycle increases. When the maximum normal opening increases the minimum opening reaches positive values, i.e. the cohesive element does not close anymore, even during cycles 137–140.

The maximum normal opening per cycle, $\max(\Delta_n)$, is shown for both sets of cohesive elements in figure 6.8 (b). For set 2, it initially increases slowly with an average of $\sim 0.025\%$ per cycle. During cycles $14-20$ the maximum opening decreases before increasing rapidly after cycle 20.

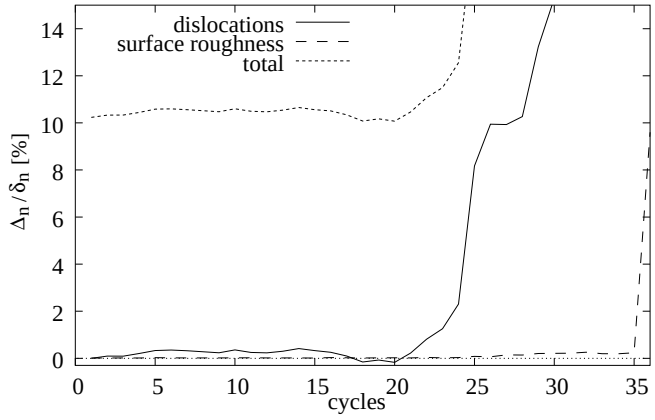

Figure 6.9: Contribution of the dislocation distribution and the surface roughness to the opening at the free surface for set 2. The total opening is caused by the elastic deformation, the dislocation distribution and the surface roughness.

In figure 6.9 the contribution of the dislocation distribution and the surface roughness to the normal opening of the cohesive element is shown for the second set of cohesive elements. Since there are only a few dislocations, the opening in the first cycle is assumed to be entirely elastic. Moreover, the elastic opening $\mathbf{\Delta}_e$ is constant during the simulation. Therefore, the contribution of the dislocations is $\tilde{\mathbf{\Delta}} + \hat{\mathbf{\Delta}} - \mathbf{\Delta}_e$ and this contribution is initially very small. However, it increases and reaches large positive values shortly before crack initiation. The contribution of the surface roughness $\bar{\mathbf{\Delta}}$ is small during most of the simulation, and increases only right before fracture initiation. This despite the fact that we placed the first cohesive element at the intersection of the most active slip plane with the free surface to maximize the contribution of the surface roughness.

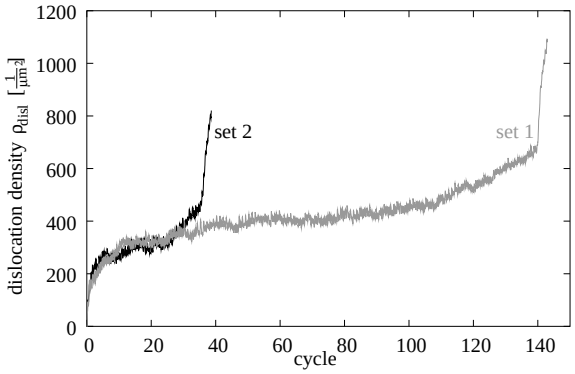

Figure 6.10: Evolution of dislocation density for both sets of cohesive elements.

The dislocation density evolution for both simulations is shown in figure 6.10. Similar to the findings with the stress-controlled 2DD model, presented in chapter 2, the dislocation density initially increases rapidly and afterwards the rate of growth decreases. Contrary to the stress-controlled model however, the dislocation density starts to grow again later in the simulation. For the first set of cohesive elements the dislocation density increases rapidly after roughly 100 cycles. Several cycles later the maximum cohesive opening starts to increase rapidly, as shown in figure 6.8 (b). With the rapid increase in the opening of the cohesive element the dislocation density increases even more rapidly. Finally, the average dislocation density inside the grain reaches $1000/\mu\mathrm{m}^2 = 10^{15}/\mathrm{m}^2$. This introduces another practical limitation, beside the problem of dislocations crossing the cohesive surface once $\Delta_n = \delta_n$. The dislocation density is so high that the computational costs of the simulation are enormous and continuation of the simulation unfeasible.

To look in more detail at the predicted behavior, figure 6.11 shows the normal opening at the free surface and the dislocation density for the first set of cohesive elements during the last cycles of the simulation. Until cycle 140 the opening has a constant amplitude and the average value gradually increases. Afterwards, within half a cycle, the opening increases

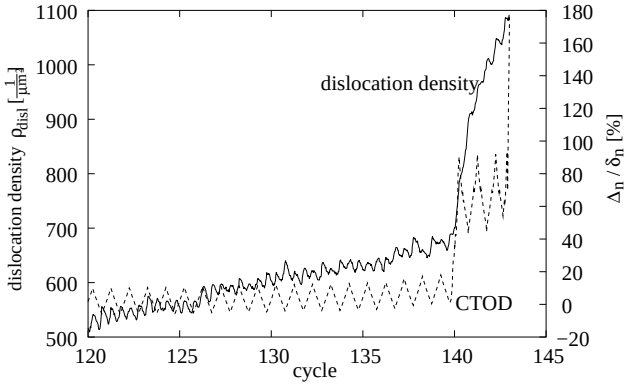

Figure 6.11: Evolution of dislocation density and normal opening at the free surface for set 1 of cohesive elements shortly before fracture initiation.

by almost 80% and the dislocation density increases as well. During cycles $141 - 143$ the maximum normal opening stays almost constant while the dislocation density increases faster than before cycle 140, although not monotonically as during cycle 140.

So far we have looked at the total dislocation density, but the dislocation distribution is not uniform. In figure 6.12 the dislocation distribution after 142 cycles obtained with the first set of cohesive elements is shown. Many dislocations have clustered in an area close to the cohesive elements. Moreover, two primary slip planes, i.e. those at $45°$, contain a very large number of dislocations. The upper left-hand corner and the grain boundary have a much lower dislocation density. The cohesive element cannot correctly take into account the elastic fields of the large number of dislocations close to the cohesive element due to the low number of integration points used in the simulation.

It should be pointed out, though, that the high density of dislocations around the cohesive element causes a numerical stability problem. In the few cycles preceding crack initiation the opening shows spikes. Within a time step the normal opening at the free surface might increase or decrease by several multiples of the Burgers vector; a few time steps later the opening jumps back. The number of these spikes and their height increase with increasing normal opening and increasing dislocation density. The reason for this numerical problem lies again in the difference between the configuration of the cohesive element and the dislocation distribution. This instability can be neglected, since it only occurs in the last cycles preceeding fracture initiation. Furthermore, for the clarity of the figures, these spikes are not shown.

The deformed grain is shown in figure 6.13. On the left-hand side of the surface a protrusion has developed in conjunction with the pronounced primary slip. The remainder of the free surface has moved inward. The principal stresses are high close to the free

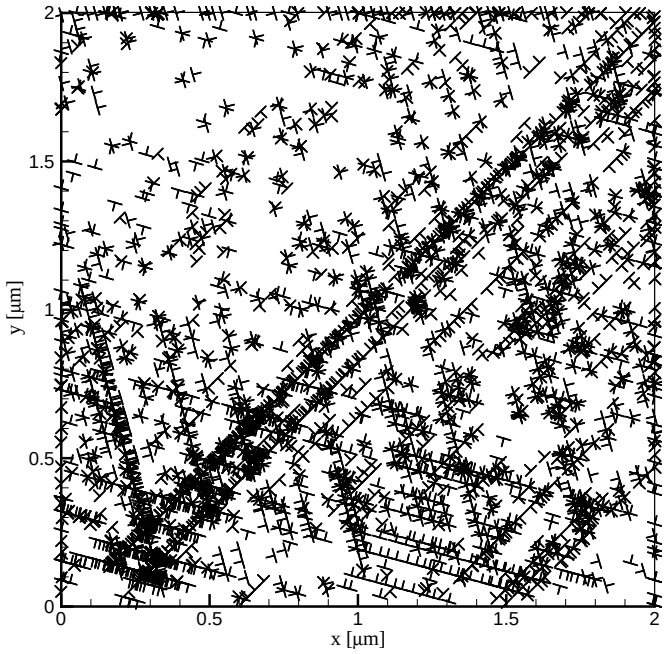

Figure 6.12: Dislocation distribution for a grain with the first set of cohesive elements after 142 cycles.

surface. The cohesive element, which is parallel to the primary slip system, has only a normal opening. Therefore, this model predicts that fatigue initiation is associated to mode I crack opening and not to mode II, as commonly believed.

The strength of the cohesive surface, $\sigma_{\max} = 600\mathrm{MPa}$, is not reflecting actual bond properties even though the normal fracture energy $\Phi_n = 1.63\mathrm{J/m}^2$ is realistic (cf. the fatigue crack growth simulations in [3]). It is much lower to allow for the simulation to finish in the given time. Therefore, the number of cycles to reach fatigue crack initiation is much smaller than those found in experiments. With a larger cohesive surface strength the material is expected to break later. With the values used here, the QuoVaDis model predicts a crack, as shown in figure 6.13, and therefore is able to simulate fatigue crack initiation.

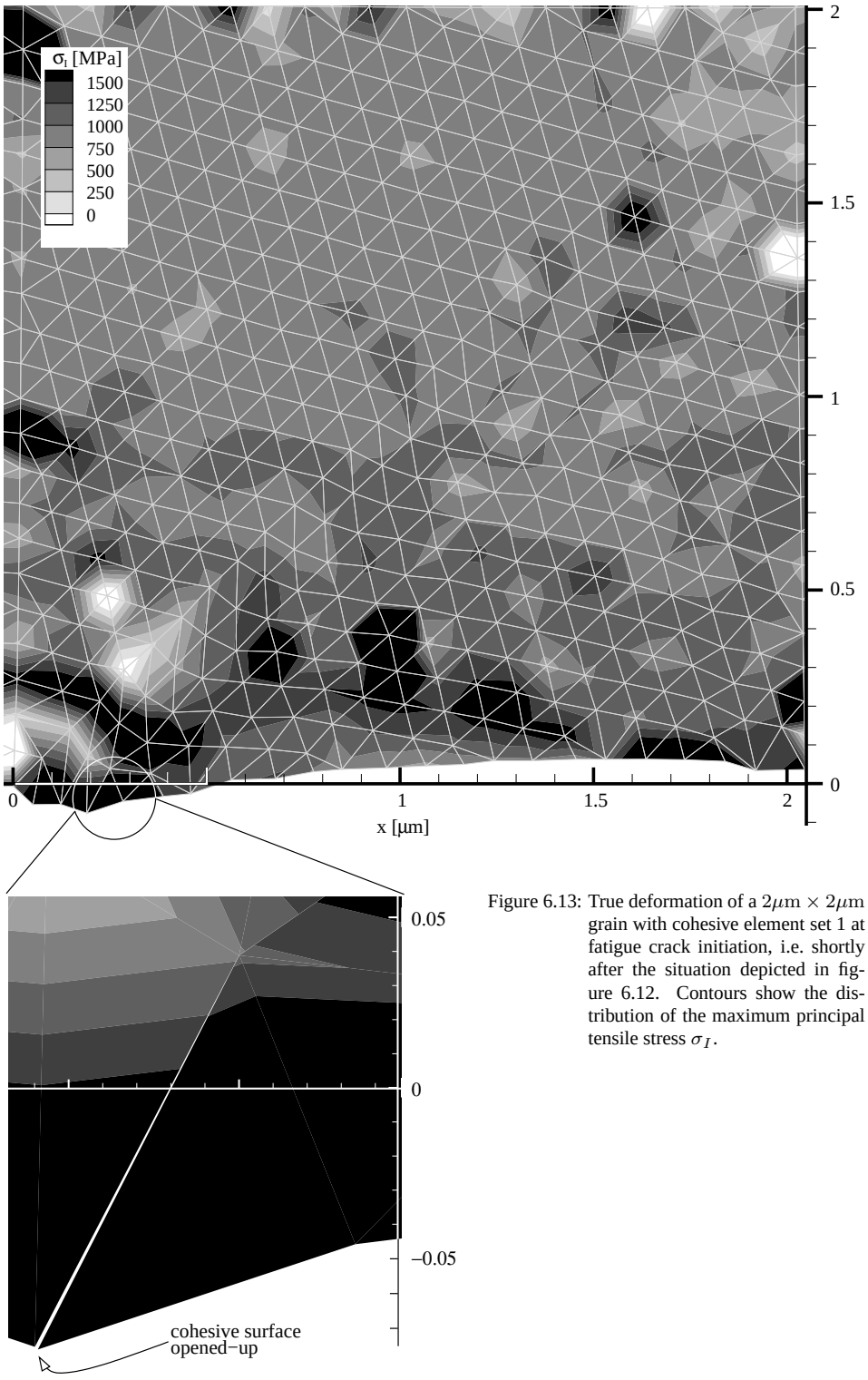

Figure 6.13: True deformation of a $2\mu\mathrm{m} \times 2\mu\mathrm{m}$ grain with cohesive element set 1 at fatigue crack initiation, i.e. shortly after the situation depicted in figure 6.12. Contours show the distribution of the maximum principal tensile stress σ_I.